



HAL
open science

Kinetics of methane hydrate formation and dissociation in sand sediment

Thi Xiu Le, Stéphane Rodts, David Hautemayou, Patrick Aimedieu, Michel Bornert, Baptiste Chabot, Anh Minh A.M. Tang

► **To cite this version:**

Thi Xiu Le, Stéphane Rodts, David Hautemayou, Patrick Aimedieu, Michel Bornert, et al.. Kinetics of methane hydrate formation and dissociation in sand sediment. *Geomechanics for Energy and the Environment*, 2020, pp.100103. 10.1016/j.gete.2018.09.007 . hal-02171357

HAL Id: hal-02171357

<https://enpc.hal.science/hal-02171357>

Submitted on 2 Jul 2019

HAL is a multi-disciplinary open access archive for the deposit and dissemination of scientific research documents, whether they are published or not. The documents may come from teaching and research institutions in France or abroad, or from public or private research centers.

L'archive ouverte pluridisciplinaire **HAL**, est destinée au dépôt et à la diffusion de documents scientifiques de niveau recherche, publiés ou non, émanant des établissements d'enseignement et de recherche français ou étrangers, des laboratoires publics ou privés.

1 **Kinetics of methane hydrate formation and dissociation in**
2 **sand sediment**

3

4 Thi Xiu Le, Stéphane Rodts, David Hautemayou, Patrick Aimedieu, Michel Bornert,
5 Baptiste Chabot, Anh Minh Tang

6 Laboratoire Navier (UMR8205 IFSTTAR-ENPC-CNRS), Université Paris Est, Marne-
7 la-vallée, France

8

9 **Corresponding author:**

10 Dr. Anh Minh TANG

11 *Ecole des Ponts ParisTech*

12 6-8 av. Blaise Pascal, Cité Descartes, Champs-sur-Marne

13 F-77455 Marne – la – Vallée cedex - France

14 E-mail: anhminh.tang@enpc.fr

15 **Abstract**

16 Methane hydrate is being considered as a potential future energy source but also a
17 considerable geo-hazard. In this study, methane hydrate bearing sand sediment was
18 firstly created by pressurizing methane gas into already chilled moistened packed sand
19 specimen (excess gas method). The excess gas was then replaced by water at high
20 pressure. Afterward, a heating/cooling cycle was applied under undrained conditions
21 in order to completely dissociate gas hydrates and then recreate them inside the
22 specimen. Finally, the pore pressure was reduced to zero to dissociate the gas
23 hydrates. The whole process was performed in a magnetic resonance imaging (MRI)
24 system allowing the determination of water and/or gas and hydrate quantity (and
25 spatial distribution) at various times. The MRI signal was finally analyzed to interpret
26 various processes in sand sediment: initial hydrate formation, heating-induced hydrate
27 dissociation, cooling-induced hydrate re-formation, and depressurizing-induced
28 hydrate dissociation.

29

30 **Keyword:** gas hydrate bearing sand sediment, dissociation/formation, kinetics,
31 magnetic resonance imaging.

32

33 **1. Introduction**

34 Natural gas hydrates (primarily methane hydrates forming naturally at high pressures
35 and low temperatures) are nowadays being considered as an alternative energy
36 source [1]. Among the existing methods of gas recovery from hydrates,
37 depressurization method is being considered as the most economically promising
38 method [2]. This method, conducted by lowering the pressure in overlying sediments,
39 may be hampered by the formation of ice and/or the reformation of gas hydrates (GH)
40 because of the endothermic cooling nature of GH. Fundamental understandings of
41 hydrate dissociation kinetics models are essential to predict hydrate reservoir
42 dissociation process in the objective of selecting appropriate hydrate bearing zones
43 and estimating gas production behavior before execution of any field tests. Some
44 kinetics models were developed to simulate the production process based on
45 heat/mass transfer and/or intrinsic kinetics of hydrate decomposition and/or gas-water
46 two-phase flow [3,4]. Different assumptions were used, their applicability to reservoir
47 level studies is also limited case by case. Various GH reservoir simulators
48 (computational tools taking into account the complex highly-coupled transport
49 equations, the reaction kinetics, the phase transition and the physical/chemical
50 properties of hydrate bearing sediment) are being developed [5,6]. The accuracy of
51 reservoir model needs, however, to be improved and the availability of long-term field
52 production test data is so important. Two successful offshore field tests (together with
53 two onshore field tests in Mount Elbert – Alaska and Malik in 2007 [7]), up to now, used
54 the depressurization method. The first offshore methane hydrate production test was
55 conducted by Japan Oil, Gas, and Metals National Corporation (JOGMEC) in the
56 eastern Nankai Trough. Approximately 120,000 m³ of methane gas (20,000 m³/day)
57 was produced by lowering pressure from 13.5 MPa to 4.5 MPa. The production was

58 interrupted due to an unexpected increase in sand production [8]. Recently in 2017,
59 the China Geological Survey extracted 120,000 m³ of gas from natural gas hydrate
60 deposits in the Shenhu area with a methane concentration of 99.5 percent (Xin Z.
61 China wraps up combustible ice mining trial, setting world records. Xinhua.
62 Guangzhou, 09 July 2017). As production costs are still high, an economically feasible
63 way to exploit gas hydrate on a large scale should be found to commercialize the
64 production of the natural gas hydrate. As it is challenging to get intact cores of methane
65 hydrate-bearing sediments, most the experimental works concern laboratory tests on
66 synthetic specimens to investigate hydrate dissociation rate, pressure-temperature
67 evolution [9–13]. The experimental reactor scale is a crucial factor; a larger reactor
68 better mimics actual field conditions but it would be more difficult to ensure the
69 homogeneity of synthesized specimens [14].

70

71 In the objective of creating synthetic methane hydrates in sandy sediments, some
72 methods were proposed and well-studied as: dissolved gas [15], partial water
73 saturation [16], excess water [17] or ice-seeding [18]. Among them, dissolved gas and
74 water excess method are supposed to form non-cementing hydrate habit in sandy
75 sediments. However, dissolved gas is time-consuming method especially at high
76 hydrate saturation because of low solubility of methane gas in water [15]. In addition,
77 methane hydrate is observed form heterogeneously inside the sample by using water
78 excess method by mean of X-Ray Micro-Tomography [19] and measures of pressure
79 at different positions in the sample [20]. Recently, Choi et al. [21] proposed an efficient
80 and consistent method by combining the partial water saturation, saline water injection
81 at restricted conditions and a temperature cycle. However, V_P after the heating process

82 is quite high while sample is not saturated. The hydrate dissociation is perhaps not
83 finished before the hydrate reformation.

84

85 Besides elastic wave velocity measurement [18,22–24] and synchrotron X-ray
86 computed tomographic microscopy [25,26], which are used to study the kinetics and
87 mechanisms of hydrate formation and dissociation, ¹H Nuclear magnetic resonance
88 spectroscopy (NMR), in particular Magnetic Resonance Imaging (MRI) (at
89 macroscopic scale of NMR) is a well-suited mean to quantitatively/qualitatively follow
90 these kinetics. In most MRI studied cases, glass beads were used to simulate the
91 porous media to investigate the tetrahydrofuran (THF), carbon dioxide (CO₂) hydrate
92 formation and dissociation [27,28]. Methane hydrate formation (by dissolved gas or
93 partially water saturation methods) was observed via Mean Intensity (*MI*) evolution and
94 2D images [29,30]. Effects of different sizes of glass beads on hydrate growth stage
95 were investigated. In general, hydrate growth rate increases when the size of the
96 porous media decreases. In addition, three growth stages of methane hydrates formed
97 after the partially water saturation method were observed: the initial growth, the rapid
98 growth and the steady stage. In sandstone media, methane hydrate formation and
99 spontaneous conversion of methane to CO₂ hydrate were studied by mean of *MI* and
100 3D images [31,32]. As time is needed to take 3D images, spatial distribution of
101 specimen during the hydrate formation was not measured regularly. The formation of
102 methane hydrates in unconsolidated bed of silica with different size ranges was
103 investigated by following the *MI* evolution, measured on vertical and horizontal slices
104 [33]. The formation was observed non-uniform and occurred at different times and
105 different positions. In addition, by using different water saturations, hydrate formation
106 was found to be faster for lower water content. The methane hydrate formation,

107 dissociation and reformation in partially water saturated Ottawa sand at different water
108 saturations were studied by combining measurements of M/I and elastic velocities [34].
109 M/I profiles along the specimen axis after these three procedures (hydrate formation,
110 dissociation and reformation) show an almost homogenous distribution of GH. The fact
111 of consolidating unsaturated sand makes water distributed more homogeneously before
112 the gas hydrate formation. The effect of depressurizing range and rate on methane
113 hydrate dissociation, in particular, the hydrate reformation and ice generation due to
114 fast depressurizing rate were observed [35,36].

115

116 In this study, methane hydrate formation based on the method proposed by Choi et al.
117 [21], but modified to improve the heating-cooling process and to adapt better with
118 existing facilities is investigated in the objective of following the specimen homogeneity
119 during the whole GH formation phase. In addition, GH dissociation after
120 depressurization method is observed. Methodological efforts were put in getting fast
121 enough measurements to follow the kinetics of GH formation/dissociation during
122 transitory steps.

123 **2. Experimental method**

124 **2.1. Materials**

125 The soil used in this study is Fontainebleau silica sand (NE34). It consists of poor-
126 graded sub-rounded grains having diameter ranging from 100 to 300 microns (see the
127 grain size distribution curve in Figure 1 obtained by laser diffraction analysis). The
128 physical characteristics of this material are detailed in Table 1. Tap water and methane
129 gas with 99.995% of purity were used in the tests.

130 **2.2. Experimental setup**

131 The schematic views of experimental setup are presented in Figure 2. The sand
132 specimen (1), 38 mm in diameter and 76 mm in height, is covered with a neoprene
133 membrane (2). The confining pressure is applied to the specimen by a
134 volume/pressure controller (7) using a perfluorinated oil (Galden®) as confining fluid
135 (3), chosen due to its low signal intensity in MRI measurements. Methane gas is
136 injected via the bottom inlet (5) by a pressure controller connected to a gas flowmeter
137 (10). The top inlet (6) is closed in this study. A second volume/pressure controller (12)
138 is used to control the water pore pressure. The specimen temperature is controlled by
139 circulating a perfluorinated oil (Galden®), which is connected to a cryostat (8), around
140 the cell (4). The cell is installed in a nuclear magnetic resonance imaging system (13)
141 for observations.

142

143 Proton (^1H) NMR/MRI measurements are performed at a Bruker 24/80 DBX
144 spectrometer operating at 0.5T (21MHz proton frequency) equipped with:

145 - A birdcage RF coil 20cm in diameter and height where the whole pressure cell
146 can fit

147 - A BGA-26 gradient system delivering a maximum gradient strength of 50mT/m
148 with a rising time of 500 μs .

149

150 Measurement protocols used in this work rely on well-established methodology. They
151 consist of:

152 - A pulse acquisition sequence, where the overall NMR signal owing to hydrogen
153 is measured after a dead time of 40 μs following the exciting RF pulse. This
154 signal is referred to as 'FID INTENSITY' signal hereafter.

155 - A 1D profile imaging based on spin-echo acquisition with a read-out gradient
156 orientated in the vertical direction and an echo time of 4.2ms, which provides
157 profile measurements with 200 pixels covering a field of view of 20cm, being
158 large enough to avoid any image aliasing owing to some parts of the external
159 set-up to the observation zone. It provides a space-resolved view of the
160 contribution

161 In both kinds of measurement, the signal intensity is expected to be proportional to the
162 amount of hydrogen atoms owing to either liquid (water) or gas (methane) phases.
163 Note that due to the Curie-law for spin polarization, the signal intensity is also inversely
164 proportional to the absolute temperature in °K of the sample. The dead-time and the
165 echo time are regarded as short enough to neglect bias owing to spin-spin relaxation.
166 On the contrary, the gas-hydrate phase, and ice phase are negligible due to its short
167 spin-spin relaxation time. Let us emphasize that FID intensities do not correspond
168 directly to profile intensities, since the integration relationship between them depends
169 on other parameters such as the sample size and the fluid amount out of the sample.
170 Related data are then presented on independent scales.

171

172 If any, the related data processing relied on home-made routines under Scilab.

173 **2.3. Test procedure**

174 Methane hydrate bearing sediment (MHBS) specimens were prepared by the following
175 procedure:

176 - Step 1 - Compaction: A determined quantity of moist sand (having known
177 moisture content) is tamped in layers to obtain a specimen with a void ratio of
178 0.63 inside the neoprene membrane before the assembly of the experimental
179 setup as shown in Figure 2.

- 180 - Step 2 - Consolidation: The confining pressure is increased to 25 MPa then
181 decreased to 10 MPa).
- 182 - Step 3 – Hydrate creation: The temperature of the cell is decreased to 2 °C.
183 Vacuum is then applied to eliminate pore air in the specimen prior to the injection
184 of methane gas at 7 MPa of pressure.
- 185 - Step 4 – Water saturation: The valve V_2 is opened to atmosphere during a short
186 period to let all the excess methane gas (initially under a pressure of 7 MPa)
187 escape from the specimen (pore pressure decreases to zero), this valve is
188 closed after that. Expecting that gas hydrates do not dissociate during this short
189 period. The valve V_1 is then immediately opened, the bottom inlet is connected
190 to the volume/pressure controller (12) to inject tap water (at ambient
191 temperature) fixed at 7 MPa of pressure to the sample. This procedure is used
192 to replace the excess gas in the specimen by water while minimizing the
193 disturbance of methane hydrates that already exist inside the specimen. Gas
194 hydrate pressure – temperature conditions are the same as that at the end of
195 step 2. Skempton's coefficient is measured at the end of this step to make sure
196 that the sample is fully saturated.
- 197 - Step 5 – Heating-induced hydrate dissociation: From this step, the confining
198 pressure is imposed to be always 3 MPa higher than the pore pressure. The
199 pore pressure is first decreased from 7 MPa to 4 MPa. The drainage valve (V_1)
200 (V_2 is always closed) is then closed and the temperature of the cell is increased
201 up to higher than 25 °C. This aims at heating the specimen under undrained
202 condition to dissociate the existing gas hydrate progressively. Note that the pore
203 pressure at the end of this step is higher for higher initial hydrate saturation. In
204 addition, the capacity of pore pressure sensor in this study is limited at 19MPa.

205 The pore pressure is increased to 19 MPa at the end of this step so that this
206 test procedure can be always feasible regardless of the hydrate saturation.

207 - Step 6 – Cooling-induced hydrate re-formation: The cell temperature is
208 decreased to 2 °C while the pore pressure is maintained constant at 19 MPa by
209 injecting water from the volume/pressure controller (12) into the sample. In the
210 objectives of reforming gas hydrates faster, this provides also the same final
211 pressure - temperature conditions for gas hydrates in the end for all tests.

212 - Step 7 – Depressurization-induced hydrate dissociation: The confining pressure
213 is maintained at 22 MPa while the valve V_2 is opened to decrease the pore
214 pressure. The volume of methane dissociated from the specimen is measured
215 by the system (9) composed also a gas/water separator and a gas collection
216 system.

217 The steps 3 – 7 are performed in the MRI system and the data are logged automatically
218 during these steps.

219 **2.4. Calibration tests**

220 Calibration tests were performed at 2°C on the compacted specimen of the first test,
221 the density of which was also very similar to that of test 2, saturated with pure phases
222 of various fluids: (a) vacuum; (b) methane gas at 7 MPa of pressure; (c) water at 7
223 MPa of pressure; (d) and water at 19 MPa of pressure. In Figure 3, *FID INTENSITY*
224 obtained for the whole system in each case is plotted. The values corresponding to
225 methane gas at 7 MPa of pressure, water at 7 MPa of pressure, and water at 19 MPa
226 of pressure were then calculated by subtracting that corresponding to the system
227 containing vacuum, in order to remove the spurious signal owing to the pressure cell
228 and the imperfectly perfluorinated oil. In the working conditions of the present study,
229 and as far as the temperature is not modified, the corrected signal is directly

230 proportional to the total amount of hydrogen atoms contained in the fluid molecules.
231 The corrected values of *FID INTENSITY* are also plotted in the Figure 3. Note that the
232 signal for pure methane is significantly smaller than that for water due to the different
233 density and chemical composition. In the subsequent sections, the corrected values of
234 *FID INTENSITY*, i.e. *FID INTENSITY* measured minus *FID INTENSITY* obtained from
235 the case (a), are shown.

236 **2.5. Test program**

237 Two tests were performed in this study with the same procedure and the same
238 parameters to ensure the repeatability of the results. The water saturation obtained
239 after compaction equals to 25% (corresponding to a moisture content of 6%).

240 **3. Experimental results and Discussions**

241 **3.1. Hydrate creation**

242 Figure 4 (a) shows the evolution of *FID INTENSITY* during hydrate formation (step 3)
243 for the two tests. When methane gas is injected into the specimen, *FID INTENSITY*
244 increases slightly during the first minutes then decreases continuously; the relationship
245 between *FID INTENSITY* and logarithm of time during the decrease phase can be
246 correlated with a linear function. After $t = 40$ h *FID INTENSITY* remains constant. The
247 results obtained by the two tests look similar even if during the first test, the data were
248 not recorded during the first minutes. The increase of *FID INTENSITY* during the first
249 minutes can be explained by the accumulation of methane gas inside the specimen
250 when the gas pressure was increasing until it reached the target value (7 MPa), see
251 Figure 4 (b) where gas pressure is plotted versus elapsed time for Test 2 (data for Test
252 1 was not available). When the gas pressure exceeds the conditions required to create
253 gas hydrate (3 MPa at 2 °C), gas hydrates start to be created inside the specimen.

254 This phenomenon decreases the quantity of water and increases the quantity of gas
255 hydrates. That explains why gas hydrate formation decreases the total *FID*
256 *INTENSITY*. Note that the intensity related to gas hydrate is negligible [31].

257

258 The following equation is used to estimate hydrate saturation (S_h):

259

$$S_h = 1.1 \frac{I_0 + I_m - I}{I_0 + 0.1 \frac{S_{wo}}{1 - S_{wo}} I_m} S_{wo} \times 100\%$$

260 Where I_0 is the initial FID intensity of the moist sand specimen and S_{wo} is the initial
261 water saturation ($S_{wo} = 25\%$). The remaining void (about 75% of total void) contents
262 methane gas (at 7 MPa of pressure when this pressure is reached). For this reason, I_m
263 - the FID intensity of methane gas (at 7 MPa of pressure) in the specimen before the
264 hydrate formation, equals to 75% of the value obtained from the calibration test (case
265 (b)): $I_m = 0.75 \times 1000 = 750$. This equation is applicable only when the gas pressure
266 equals 7 MPa. The underlying assumption for this equation is that water reacts locally
267 to form hydrates, and that gas can go in and out of the sample to occupy the remaining
268 space between hydrates and remaining water, owing to the 10% of volume increase
269 when water is converted to hydrate. As a result, during the hydrate formation, the
270 remaining void containing methane gas is $(100 - S_{wo} - S_h)\%$ of total void.

271

272 Figure 4 (c) shows the estimated hydrate saturation evolution for Test 2. Hydrate starts
273 to be created immediately when the gas pressure is higher than 3 MPa. As mentioned
274 before, hydrate saturation is only calculated from when pore pressure reaches 7MPa
275 (at 0.06th hour, hydrate saturation is 0.3%). The hydrate content increases then linearly
276 with the logarithm of time and reaches its maximal value after 40 h. Note that, after 40
277 h, $S_h = 27\%$, that means all water in the specimen has been transformed to hydrate,

278 and that the remaining NMR signal at the end of the process is that of the methane
279 phase.

280

281 Figure 5 plots the signal (*i.e.* owing to water and methane) versus the elevation ($Z = 0$
282 corresponds approximatively to the bottom of the specimen) for various times. It can
283 be noted that the signal is generally homogenous along the specimen elevation. At the
284 beginning ($t = 0$), the specimen contains only water and air in the pore space. Slight
285 fluctuation of the signal along the elevation should correspond to the compaction
286 procedure (moisture sand tamped by layers of 10 - 20 mm), which induces slight
287 heterogeneity of porosity and water distribution in the specimen. When methane gas
288 is injected into the specimen, GH is formed and the water content decreases
289 progressively. That explains why the signal decreases progressively with time and the
290 profile becomes more homogenous.

291

292 Bagherzadeh et al. [33] found that hydrate formation occurs faster in a bed with lower
293 initial water saturation and as opposed to the higher water saturation case, hydrate
294 formed homogeneously at 25% of initial water saturation. This is in agreement with
295 homogenous Z profiles during GH formation in gas saturated media in this study.

296

297 Rydzy [34] investigated the kinetics of methane hydrate formation in unsaturated
298 Ottawa sand via the combination of wave velocity measurements and MRI (Mean
299 Intensity, MI). The results showed that at low initial water saturation, MI decreased
300 quickly few hours after gas injection which means hydrate saturation increased quickly.
301 In addition, velocities (compressional and shear velocities) increased quickly during
302 hydrate saturation, slowed down and became stable from when hydrate formation was

303 almost finished. This could be explained by cementation model illustrating hydrate
304 growth in capillary water at sand grains contacts [37,38] which supposed that films of
305 hydrates are first formed quickly at water-gas interfaces, the subsequent hydrate
306 formation (from the films toward the centers of grain contacts) is slower depending on
307 the diffusion of methane molecules through the hydrate film and water. This can be
308 also used to explain the linear relationship between *FID INTENSITY* and logarithm of
309 time observed in the present study during the hydrate formation. However, in the work
310 of Rydzy [34], 5% to 12% of pore water was found to remain unconverted to hydrate
311 at the end of experiments while in the present study almost 100% of water becomes
312 hydrates. Actually, in the work of Rydzy [34], the signal of methane gas was not
313 considered and that would induce errors in water content estimation in the specimen.

314

315 **3.2. Water Saturation**

316 Figure 6 plots *FID INTENSITY* during the water saturation (Step 4). $t = 0$ corresponds
317 to the opening of the valve V_2 . That induces a quick decrease of *FID INTENSITY* to 0.
318 Afterward, when water is injected to the specimen ($t = 0.06$ h) *FID INTENSITY*
319 increases quickly and reaches the maximal value when water pressure reaches 7 MPa.
320 Water injection in Test 1 is slowed down between 0.1 – 0.4th hour due to an interruption
321 to inject more water into the volume/pressure controller (12).

322

323 The signal versus elevation is plotted at various times for the Test 2 in Figure 7. Profile
324 at 60s ($t = 0.047$ h) was measured when methane gas was decreased to the
325 atmospheric pressure. When water is injected from the bottom inlet, signal at the
326 bottom starts to increase first ($t = 0.063$ h). When the water pore pressure reaches 7
327 MPa, the specimen can be expected to be fully saturated with water, $t = 55$ h (methane

328 gas should not exist in this conditions). At this state, higher signal can be observed in
329 the zone close to the bottom of the specimen while it is lower in the zone close to the
330 top.

331
332 Figure 8 plots the signal versus elevation for both two tests at the end of the water
333 saturation step. The results of the Test 1 show also a higher signal close to the bottom
334 but the signal at the top is similar to the remaining part of the specimen. The
335 heterogeneity of water distribution at the end of this step can be explained by the
336 saturation procedure. Actually, methane gas evacuation and water injection were
337 performed both from the bottom. Methane gas evacuation, even if it was performed
338 quickly, less than one minute, would induce hydrate dissociation at the zone close to
339 the bottom. That explains why in the end, hydrate saturation at the bottom was lower
340 (higher signal) than the other parts of the specimen.

341
342 Hydrate saturation is estimated 20.5% and 27.5% respectively for two tests based on
343 intensity of water saturated sample at 7MPa. Hydrates dissociation at the zone close
344 to the bottom induces eventually the decrease of hydrate saturation compared to that
345 after hydrate creation step. However, it is the same for Test 2. When water is injected
346 from the bottom, the remaining gas would cumulate in the zone close to the top of the
347 specimen, thus impeding total water saturation. At the end of water saturation phase,
348 remaining gas would be transformed to gas hydrates, hydrate saturation in increased.
349 That is why the hydrate saturation in this zone seems higher than in the other parts
350 (lower signal) in Figure 8.

351 **3.3. GH Dissociation-Reformation**

352 As mentioned above, a temperature cycle was performed after the water saturation
353 phase. Figure 9 shows the pore pressure (a), the cryostat temperature (b) and *FID*
354 *INTENSITY* (c) versus elapsed time for Test 1. It should be noted that specimen
355 temperature could not be measured during these tests in the MRI system. However,
356 preliminary tests performed outside the MRI system showed a characteristic time of 20
357 min for the temperature exchange between the cryostat and the specimen. At the
358 beginning of the tests, the pore pressure is first decreased to 4 MPa for a faster
359 heating-induced gas hydrate dissociation as gas hydrates are closer to equilibrium
360 boundary. Note that heating gas hydrates in undrained conditions induced the increase
361 of pore pressure (close to corresponding equilibrium pressure of gas hydrates) mainly
362 due to thermal dilation of water and hydrate dissociation [39]. Afterward, the cryostat
363 temperature is increased from 2 °C to 25 °C with a constant rate. As heating is
364 performed under undrained conditions (the valves V_1 and V_2 were closed), pore
365 pressure increases according to heating and stabilizes at 14 MPa when the
366 temperature reaches 25 °C. Heating-induced pore pressure increase is mainly due to
367 thermal dilation of water and hydrate dissociation [39]. After this phase, the valve V_1 is
368 opened to connect the cell to the pressure/volume controller (No. 12 in Figure 2) in
369 order to impose a pore pressure of 19 MPa. This pressure is maintained until the end
370 of the cooling-induced hydrate re-formation phase (Step 6). At $t = 7.5$ h, the cell
371 temperature is decreased quickly to 2 °C to re-create GH.

372

373 Figure 9 (c) plots *FID INTENSITY* versus elapsed time during these steps. The data
374 from the beginning to $t = 1.6$ h was unfortunately not available. From $t = 1.6$ h, *FID*
375 *INTENSITY* decreases as the specimen temperature increases. Note that owing to

376 Curie law for spin polarization in the MRI magnet, *FID INTENSITY* must be here
377 considered to be additionally influenced by temperature, being inversely proportional
378 to its absolute value in Kelvin. For a given fluid content, it then increases when
379 temperature decreases and vice versa. At $t = 2.8$ h, *FID INTENSITY* starts to increase
380 when the signal of water creation (from dissociated GH) was higher than that induced
381 by temperature increase. In the present study, no direct temperature measurement
382 was available inside the specimen, and no temperature correction of *FID INTENSITY*
383 was made. At $t = 3.6$ h, *FID INTENSITY* decreases when GH has been completely
384 dissociated (pore pressure reached 14 MPa) but the specimen temperature continues
385 to increase to reach the imposed temperature in cryostat. At $t = 4.4$ h, increasing pore
386 pressure from 14 MPa to 19 MPa induces an increase of *FID INTENSITY*. When the
387 cryostat temperature is decreased quickly ($t = 7.5$ h), the temperature of the specimen
388 decreases progressively inducing an increase of *FID INTENSITY*. At $t = 8.2$ h, GH
389 starts to be re-created progressively inducing decrease of *FID INTENSITY*. When the
390 GH re-creation is completed, *FID INTENSITY* stabilizes.

391
392 The results of the Test 2 are shown in Figure 10. After reducing the pore pressure from
393 7 MPa to 4 MPa, the cryostat temperature is increased quickly from 2 °C to 20 °C ($t =$
394 0.1 h) and then to 25 °C ($t = 2.1$ h). It is decreased to 2 °C at $t = 22$ h. Heating under
395 undrained conditions induces an increase of pore pressure from 4 MPa to 15 MPa.
396 The subsequent heating (from 20 °C to 25 °C) does not influence the pore pressure.
397 From $t = 4.1$ h, the pore pressure is maintained at 19 MPa as the case of the Test 1.
398 The results on *FID INTENSITY* show phenomena similar to that observed in Test 1: $t =$
399 0 – 0.6 h, *FID INTENSITY* decreases due to heating; $t = 0.6 – 1.9$ h, *FID INTENSITY*
400 increases due to GH dissociation; $t = 1.9 – 4$ h, *FID INTENSITY* decreases due to

401 heating; from $t = 4$ h, *FID INTENSITY* increases due to increase of pore pressure (from
402 14 MPa to 19 MPa); $t = 22$ h *FID INTENSITY* increases first due to cooling then
403 decreases due to GH re-formation. More regular *FID INTENSITY* acquisitions between
404 2-5th hour are not available to reflect better the GH dissociation – reformation.

405

406 Figure 11 shows the signal versus elevation for the two tests at the end of the water
407 saturation, GH dissociation, and GH reformation phases. The results show a slight
408 redistribution of water after the GH dissociation/reformation cycle. At the end of this
409 cycle, water seems distributed more homogeneously. Min/Mean and Max/Mean profile
410 signal of Test 1 are (0.92; 1.30), (0.93; 1.10) respectively for water saturation and GH
411 reformation case. Similarly, they are (0.76; 1.32), (0.90; 1.26) for Test 2.

412

413 **3.4. Depressurization-induced hydrate dissociation**

414 To observe the depressurization-induced GH dissociation, pore pressure is first
415 decreased from 19 MPa to 5 MPa while specimen temperature is maintained at 2 °C.
416 Note that, these conditions are inside the GH stabilization zone. The valve V_2 is then
417 connected to the system (9) while the valve V_1 is closed. That reduces pore pressure
418 directly to atmospheric pressure. The quantity of dissociated methane gas measured
419 by the system (9) is used to estimate the hydrate saturation S_h remaining in the
420 specimen. MRI data are disregarded for such purpose because ice is likely to appear
421 in the specimen at this step and impede the direct interpretation of signal intensity.

422

423 Figure 12 shows hydrate saturation and *FID INTENSITY* versus elapsed time during
424 the GH dissociation for Test 1 (a) and Test 2 (b). The results of Test 1 show a quick
425 decrease of S_h from 21% at the beginning to 0 almost after 0.2 h. During this period,

426 *FID INTENSITY* decreases quickly. Once the hydrate dissociation is finished, *FID*
427 *INTENSITY* increases slowly during the next hour. The results of Test 2 show similar
428 trends but *FID INTENSITY* decreased more slowly at the beginning. In fact, in the
429 objective of decelerating the gas hydrate dissociation, for Test 2, valve V_2 was opened
430 partly at the beginning (0 - 0.067^h hour). However, hydrate dissociation was stopped
431 as created gas and water were blocked in the sample. Valve V_2 was so opened
432 completely, *FID INTENSITY* decreased fast afterward. The decrease of *FID*
433 *INTENSITY* during the hydrate dissociation phase can be explained by the expellee of
434 water from the specimen by the created methane gas. At the same time, as hydrate
435 dissociation is an endothermic process, ice would be formed during this phase. That
436 induces decrease of *FID INTENSITY* even when gas hydrates are almost dissociated.
437 In the subsequent phase, ice melting increases the quantity of liquid water in the
438 specimen, which explains the increase of *FID INTENSITY*.

439

440 The signal versus elevation is plotted for various times during this step in Figure 13.
441 These results confirm the statement above. Ice formation takes place only in the zone
442 where hydrate is present (that means along the specimen except the zone close to the
443 bottom). For this reason, signal at this zone increases at the end of the dissociation
444 phase (which corresponds to ice melting) while the signal at the zone close to the
445 bottom remains constant. Actually, rapid dissociation by depressurizing the sediments
446 below the quadruple point of methane hydrate drops the temperature below the
447 freezing point of water causing ice formation [9,10]. Heat of hydrate dissociation is 450
448 Jg^{-1} [40] while it is -342Jg^{-1} for the transformation of water at 2 °C to ice. Depending on
449 heat transfer in the temperature control system to compensate the temperature
450 decrease due to GH dissociation, GH reformation and ice formation ratio vary

451 depending also on the kinetics of GH dissociation. That is why, pore pressure is
452 reduced from 19 MPa to 5 MPa before finally set up at atmospheric pressure to better
453 observe the GH dissociation. Fan et al. 2017 [35] investigated the methane hydrate
454 dissociation in glass beads by depressurization method. Ice formation was also
455 observed by a rapid reduction of M/I and water distribution variation with time in the
456 case where pore pressure was reduced below the quadruple point of methane
457 hydrates.

458

459 To exploit natural gas hydrates after the depressurization method, the pressure in a
460 bottom hole is first lowered by a submersible pump. During the GH dissociation, GH
461 saturation decreases, low pressure is transferred to a distant region from well due to
462 dramatic increase of permeability. GH dissociation stops when reservoir temperature
463 is lower or identical to the corresponding GH equilibrium due to an endothermic
464 reaction [14]. GH reformation and/or ice formation during GH dissociation is a common
465 problem to overcome to increase the potential of hydrate production after the
466 depressurization method. Some reservoir simulators (Hydrosim, MH 21, STOMP-HYD,
467 CMG-STARS, TOUGH + HYDRATE) have been developed and are commonly used
468 [14]. However, field scale production tests are needed to improve the accuracy of
469 numerical predictions. In this study, due to the limited laboratory specimen size, the
470 high production pressure and the fast depressurizing rate, the dissociation and ice
471 formation are observed almost homogenous along the elevation. Experimental scale
472 is then one of the important factors needed to be paid attention for future laboratory
473 GH dissociation studies.

474 **Conclusion**

475 MHBS is firstly created by pressurizing methane gas (at 7 MPa) into already chilled
476 moistened packed sand specimen (after excess gas method). Following the hydrate
477 formation, water is injected into the specimen and the remaining gas is bled out
478 simultaneously. A subsequent heating/cooling cycle is applied in order to completely
479 dissociate GH and then recreate them inside the specimen. Methane hydrate
480 dissociation after the depressurization method is also investigated after the whole GH
481 formation process. From MRI measurements, the following conclusions can be drawn:

- 482 - Pressurizing methane gas into already chilled moistened packed sand
483 specimen creates GH homogenously in the specimen. The formation is fast at
484 the beginning, slows down after some hours and then stabilizes after some ten
485 hours.
- 486 - Subsequent water saturation redistributes GH in the specimen. S_h at the water
487 inlet is smaller than the other part (due to GH dissociation) while S_h at the
488 opposite end could be higher (due to additional GH formation).
- 489 - Undrained heating/cooling cycle makes the GH distribution more homogenous
490 in the specimen.
- 491 - The ice formation due to depressurization-induced GH dissociation below the
492 quadruple point of methane hydrate is observed.

493 The findings of the present work would be helpful for future studies on MHBS in
494 laboratory. The temperature cycle is considered as an essential step to reproduce
495 natural MHBS homogenously in the specimen. MRI is a good mean to investigate the
496 hydrate dissociation.

497 **Acknowledgement**

498 The authors would like to express their great appreciation to the French National
499 Research Agency for funding the present study, which is part of the project HYDRE
500 “Mechanical behavior of gas-hydrate-bearing sediments” –ANR-15-CE06-0008.
501 We also would like to express our sincere thanks to Jaime Gil Roca, Marine Lemaire
502 and Emmanuel De Laure for their technical support.

503 **References**

- 504 [1] Collett TS, Johnson AH, Knapp CC, Boswell R. Natural gas hydrates: A review.
505 *Am Assoc Pet Geol* 2009;89:146–219. doi:10.1306/13201101M891602.
- 506 [2] Collett T, Bahk J, Baker R, Boswell R, Divins D, Frye M, et al. Methane Hydrates
507 in Nature Current Knowledge and Challenges. *J Chem Eng Data* 2015;60:319–
508 29.
- 509 [3] Yousif MH, Abass HH, Selim MS, Sloan ED. Experimental and Theoretical
510 Investigation of Methane-Gas-Hydrate Dissociation in Porous Media. *Soc Pet*
511 *Eng Reserv Eng* 1991;6:69–76. doi:10.2118/18320-PA.
- 512 [4] Hong H, Bishnoi PR. Modelling of Gas Production From Hydrates in Porous
513 Media. *J Can Pet Technol* 2003;42:45–56. doi:10.2118/03-11-05.
- 514 [5] Moridis G, Collett T, Boswell R, Kurihara M, Reagan M, Koh C, et al. Toward
515 Production From Gas Hydrates: Current Status, Assessment of Resources, and
516 Simulation-Based Evaluation of Technology and Potential. *SPE Reserv Eval Eng*
517 2009;12:745–71. doi:10.2118/114163-PA.
- 518 [6] Kurihara M, Narita H, Masuda Y. Gas Production From Methane Hydrate
519 Reservoirs. *Proc. 7th Int. Conf. Gas Hydrates (ICGH 2011)*, 2011.
- 520 [7] Chong ZR, Hern S, Yang B, Babu P, Linga P, Li X. Review of natural gas
521 hydrates as an energy resource: Prospects and challenges. *Appl Energy*
522 2016;162:1633–52. doi:10.1016/j.apenergy.2014.12.061.
- 523 [8] Konno Y, Fujii T, Sato A, Akamine K, Naiki M, Masuda Y, et al. Key Findings of
524 the World's First Offshore Methane Hydrate Production Test off the Coast of
525 Japan: Toward Future Commercial Production. *Energy and Fuels*
526 2017;31:2607–16. doi:10.1021/acs.energyfuels.6b03143.
- 527 [9] Haligva C, Linga P, Ripmeester JA, Englezos P. Recovery of methane from a
528 variable-volume bed of silica sand/hydrate by depressurization. *Energy and*
529 *Fuels* 2010;24:2947–55. doi:10.1021/ef901220m.
- 530 [10] Konno Y, Uchiumi T, Oyama H, Jin Y, Nagao J, Masuda Y, et al. Dissociation
531 behavior of methane hydrate in sandy porous media below the quadruple point.
532 *Energy and Fuels* 2012;26:4310–20. doi:10.1021/ef300628c.
- 533 [11] Tonnet N, Herri JM. Methane hydrates bearing synthetic sediments-
534 Experimental and numerical approaches of the dissociation. *Chem Eng Sci*
535 2009;64:4089–100. doi:10.1016/j.ces.2009.05.043.
- 536 [12] Xiong L, Li X, Wang Y, Xu C. Experimental study on methane hydrate
537 dissociation by depressurization in porous sediments. *Energies* 2012;5:518–30.
538 doi:10.3390/en5020518.

- 539 [13] Rong Z, Yin Z, Hao J, Tan C, Linga P. Experimental investigations on energy
540 recovery from water-saturated hydrate bearing sediments via depressurization
541 approach. *Appl Energy* 2017;204:1513–25.
542 doi:10.1016/j.apenergy.2017.04.031.
- 543 [14] Xu C-G, Li X-S. Research progress on methane production from natural gas
544 hydrates. *RSC Adv* 2015;5:54672–99. doi:10.1039/C4RA10248G.
- 545 [15] Spangenberg E, Kulenkampff J, Naumann R, Erzinger J. Pore space hydrate
546 formation in a glass bead sample from methane dissolved in water. *Geophys*
547 *Res Lett* 2005. doi:10.1029/2005GL024107.
- 548 [16] Waite W., Winters WJ, Mason DH. Methane hydrate formation in partially water-
549 saturated Ottawa sand. *Am Mineral* 2004;89:1202–7.
- 550 [17] Priest JA, Rees EVL, Clayton CRI. Influence of gas hydrate morphology on the
551 seismic velocities of sands. *J Geophys Res Solid Earth* 2009;114.
552 doi:10.1029/2009JB006284.
- 553 [18] Priest JA, Best AI, Clayton CRI. A laboratory investigation into the seismic
554 velocities of methane gas hydrate-bearing sand. *J Geophys Res B Solid Earth*
555 2005;110:1–13. doi:10.1029/2004JB003259.
- 556 [19] Kneafsey TJ, Rees EVL, Nakagawa S, Kwon T. Examination of Hydrate
557 Formation Methods: Trying to Create Representative Samples. 2010.
- 558 [20] Chong ZR, Pujar GA, Yang M, Linga P. Methane hydrate formation in excess
559 water simulating marine locations and the impact of thermal stimulation on
560 energy recovery. *Appl Energy* 2016;177:409–21.
561 doi:10.1016/j.apenergy.2016.05.077.
- 562 [21] Choi J-H, Dai S, Cha J-H, Seol Y. Laboratory formation of noncementing
563 hydrates in sandy sediments. *Geochemistry, Geophys Geosystems*
564 2014;15:1648–56. doi:10.1002/2014GC005287.
- 565 [22] Rydzy MB, Batzle ML. Ultrasonic Velocities in Laboratory- Formed Gas
566 Hydrate- Bearing Sediments. *Symp. Appl. Geophys. to Eng. Environ. Probl.*
567 2010, Colorado: 2010, p. 615–24. doi:10.4133/1.3445488.
- 568 [23] Hu G-W, Ye Y-G, Zhang J, Diao S-B, Liu C-L. Acoustic Properties of Hydrate-
569 Bearing Unconsolidated Sediments Measured by the Bender Element
570 Technique. *Chinese J Geophys* 2012;55:635–47. doi:10.1002/cjg2.1758.
- 571 [24] Zhang Q, Li FG, Sun CY, Li QP, Wu XY, Liu B, et al. Compressional wave
572 velocity measurements through sandy sediments containing methane hydrate.
573 *Am Mineral* 2011;96:1425–32. doi:10.2138/am.2011.3681.
- 574 [25] Kerkar P, Jones KW, Kleinberg R, Lindquist WB, Tomov S, Feng H, et al. Direct
575 observations of three dimensional growth of hydrates hosted in porous media.
576 *Appl Phys Lett* 2009;95:2007–10. doi:10.1063/1.3120544.
- 577 [26] Chaouachi M, Falenty A, Sell K, Enzmann F, Kersten M, Haberth€ D, et al.
578 Microstructural evolution of gas hydrates in sedimentary matrices observed with
579 synchrotron X-ray computed tomographic microscopy. *Geochemistry, Geophys*
580 *Geosystems* 2014:1009–20. doi:10.1002/2013GC005162.
- 581 [27] Zhao J, Yao L, Song Y, Xue K, Cheng C, Liu Y, et al. In situ observations by
582 magnetic resonance imaging for formation and dissociation of tetrahydrofuran
583 hydrate in porous media. *ScienceDirect* 2010;29:281–8.
584 doi:10.1016/j.mri.2010.08.012.
- 585 [28] Chuanxiao C, Jiafei Z, Yongchen S, Zihao Z. In-situ observation for formation
586 and dissociation of carbon dioxide hydrate in porous media by magnetic. *Sci*
587 *China Earth Sci* 2013;56:611–7. doi:10.1007/s11430-012-4570-5.
- 588 [29] Zhao J, Yang L, Xue K, Lam W, Li Y, Song Y. In situ observation of gas hydrates

- 589 growth hosted in porous media. *Chem Phys Lett* 2014;612:124–8.
590 doi:10.1016/j.cplett.2014.07.066.
- 591 [30] Zhao J, Lv Q, Li Y, Yang M, Liu W, Yao L, et al. In-situ visual observation for the
592 formation and dissociation of methane hydrates in porous media by magnetic
593 resonance imaging. *Magn Reson Imaging* 2015;33:485–90.
594 doi:10.1016/j.mri.2014.12.010.
- 595 [31] Baldwin BA, Stevens J, Howard JJ, Graue A, Kvamme B, Aspenes E, et al. Using
596 magnetic resonance imaging to monitor CH₄ hydrate formation and
597 spontaneous conversion of CH₄ hydrate to CO₂ hydrate in porous media. *Magn
598 Reson Imaging* 2008;27:720–6. doi:10.1016/j.mri.2008.11.011.
- 599 [32] Ersland G, Husebø J, Graue A, Baldwin BA, Howard J, Stevens J. Measuring
600 gas hydrate formation and exchange with CO₂ in Bentheim sandstone using MRI
601 tomography. *Chem Eng J* 2008;158:25–31. doi:10.1016/j.cej.2008.12.028.
- 602 [33] Bagherzadeh SA, Moudrakovski IL, Ripmeester JA, Englezos P. Magnetic
603 Resonance Imaging of Gas Hydrate Formation in a Bed of Silica Sand Particles.
604 *Energy Fuels* 2011 2011;25:3083–92. doi:10.1021/ef200399a.
- 605 [34] Rydzy MB. The effect of hydrate formation on the elastic properties of
606 unconsolidated sediment. Colorado School of Mines, 2014.
- 607 [35] Fan Z, Sun C, Kuang Y, Wang B, Zhao J, Song Y. MRI Analysis for Methane
608 Hydrate Dissociation by Depressurization and the Concomitant Ice Generation.
609 *Energy Procedia*, vol. 105, Elsevier B.V.; 2017, p. 4763–8.
610 doi:10.1016/j.egypro.2017.03.1038.
- 611 [36] Zhang L, Zhao J, Dong H, Zhao Y, Liu Y, Zhang Y. Magnetic resonance imaging
612 for in-situ observation of the effect of depressurizing range and rate on methane
613 hydrate dissociation. *Chem Eng Sci* 2016;144:135–43.
614 doi:10.1016/j.ces.2016.01.027.
- 615 [37] Kneafsey TJ. Repeated Methane Hydrate Formation and Dissociation in a
616 Partially Water Saturated Sand: Impact on Hydrate Heterogeneity and Sonic-
617 Frequency Seismic Properties. 7th Int. Conf. Gas Hydrates (ICGH 2011), 2011.
- 618 [38] Pinkert S, Grozic JLH. Failure mechanisms in cemented hydrate-bearing sands.
619 *J Chem Eng Data* 2015;60:376–82. doi:10.1021/je500638c.
- 620 [39] Kwon TH, Cho GC, Santamarina JC. Gas hydrate dissociation in sediments:
621 Pressure-temperature evolution. *Geochemistry, Geophys Geosystems*
622 2008;9:1–14. doi:10.1029/2007GC001920.
- 623 [40] Garg SK, Pritchett JW, Katoh A, Baba K, Fujii T. A mathematical model for the
624 formation and dissociation of methane hydrates in the marine environment. *J
625 Geophys Res Solid Earth* 2008;113:1–32. doi:10.1029/2006JB004768.
- 626 [41] Feia S, Dupla JC, Ghabezloo S, Sulem J, Canou J, Onaisi A, et al. Experimental
627 investigation of particle suspension injection and permeability impairment in
628 porous media. *Geomech Energy Environ* 2015;3:24–39.
629 doi:10.1016/j.gete.2015.07.001.
- 630
631

632

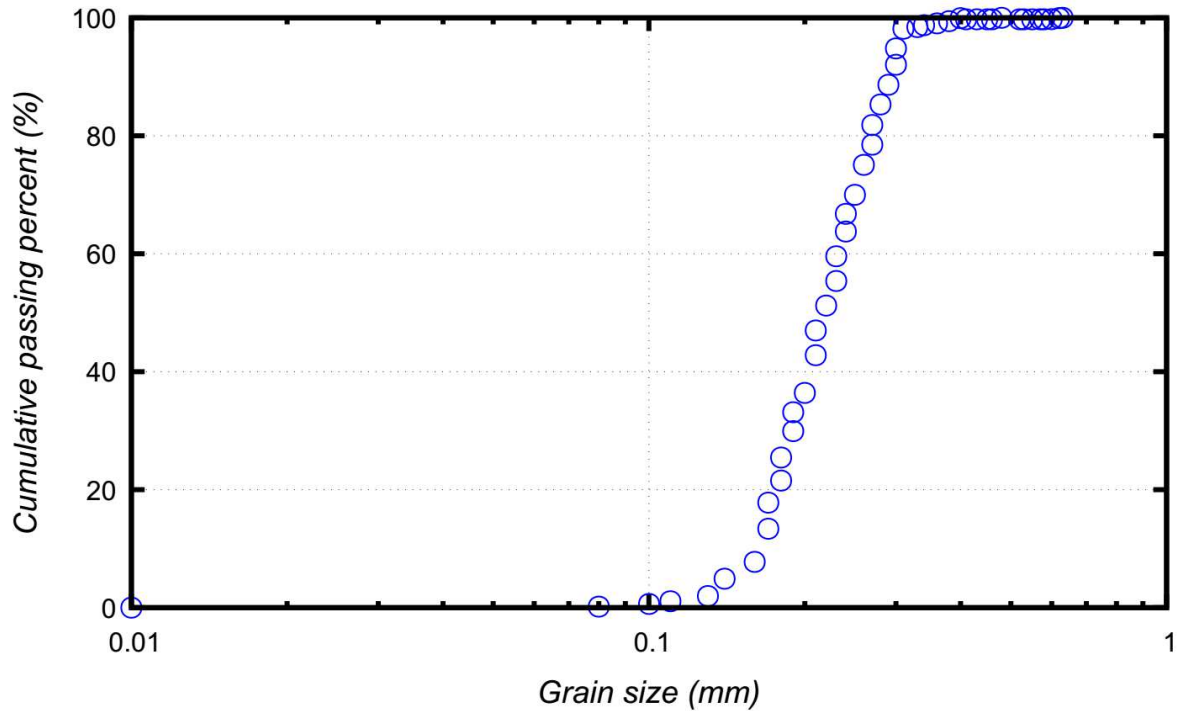
Table 1. Characteristics of Fontainebleau sand [41]

Material	d_{50} (mm)	d_{10} (mm)	e_{min}	e_{max}	Angularity	ρ_s (Mg/m ³)
Fontainebleau sand	0.206	0.150	0.56	0.88	Sub-rounded	2.65

633 d_{10}, d_{50} : grain sizes corresponding to 10, 50 % passing respectively; e_{min}, e_{max} : minimum
634 and maximum void ratio respectively; ρ_s grain mass density.

~~635~~

637

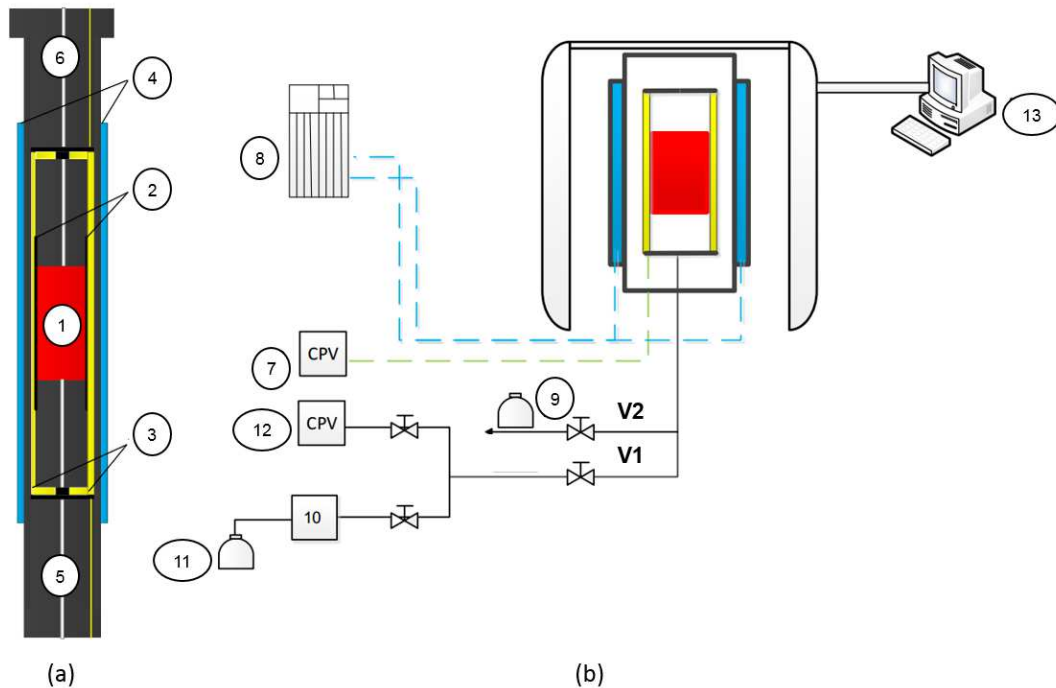


638

639

Figure 1. Particle size distribution (modified from [37])

640



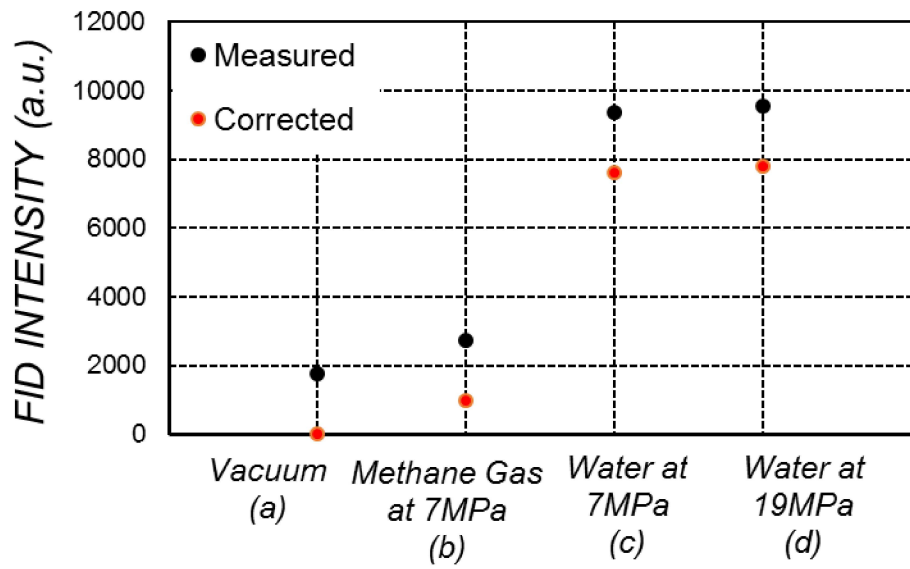
641

642 1 - Sand specimen; 2 - Neoprene membrane; 3 - Confining fluid; 4 - Temperature
 643 controlling fluid; 5 - Bottom inlet; 6 - Top inlet; 7 - Confining CPV; 8 - Cryostat; 9 -
 644 System to measure volume of gas; 10 - Gas flowmeter; 11 - CH₄ bottle; 12 - Water
 645 CPV; 13 - MRI measured system.

646

Figure 2. Schematic diagram of the experimental setup

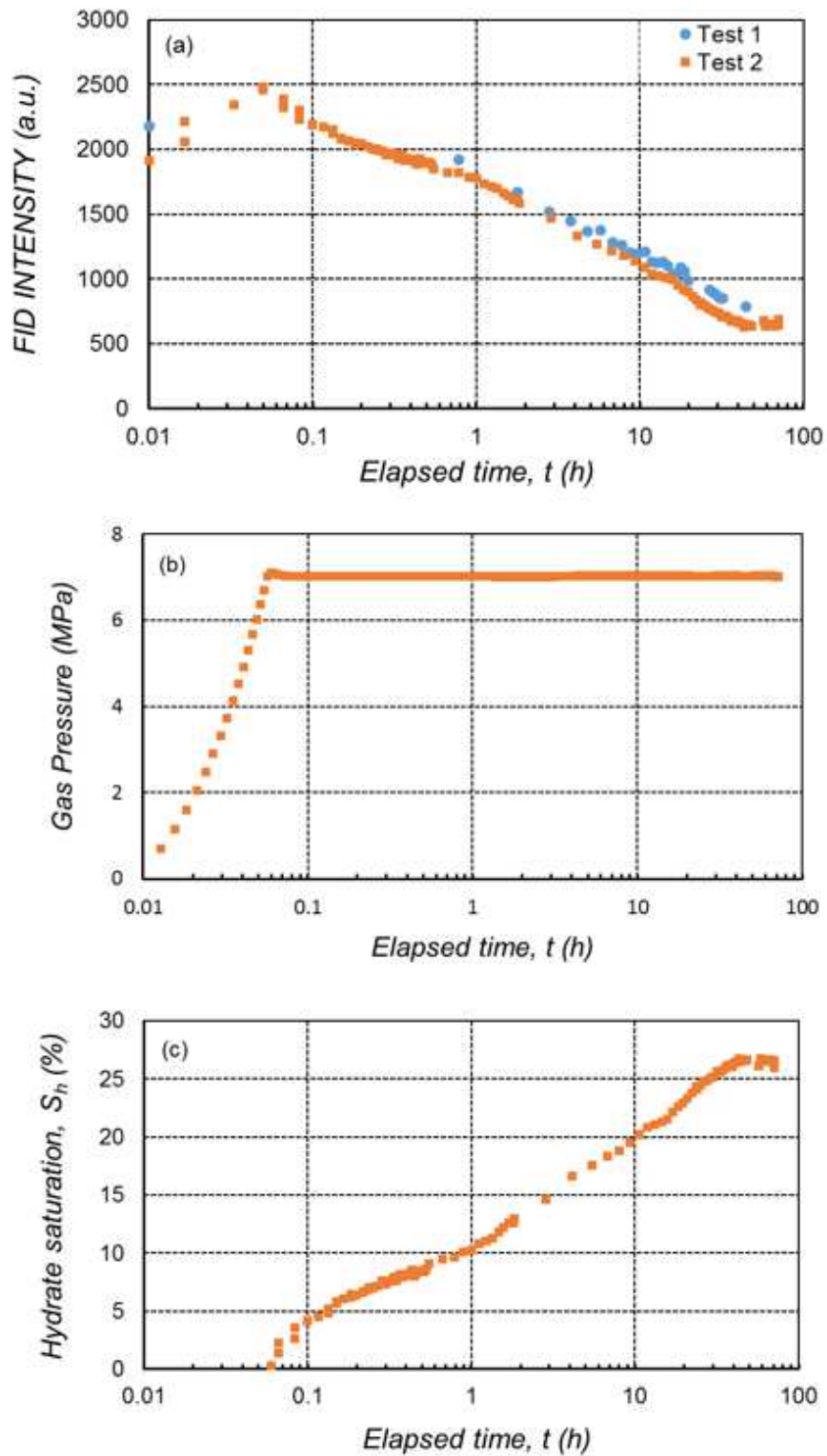
647



648

649

Figure 3. Reference signal

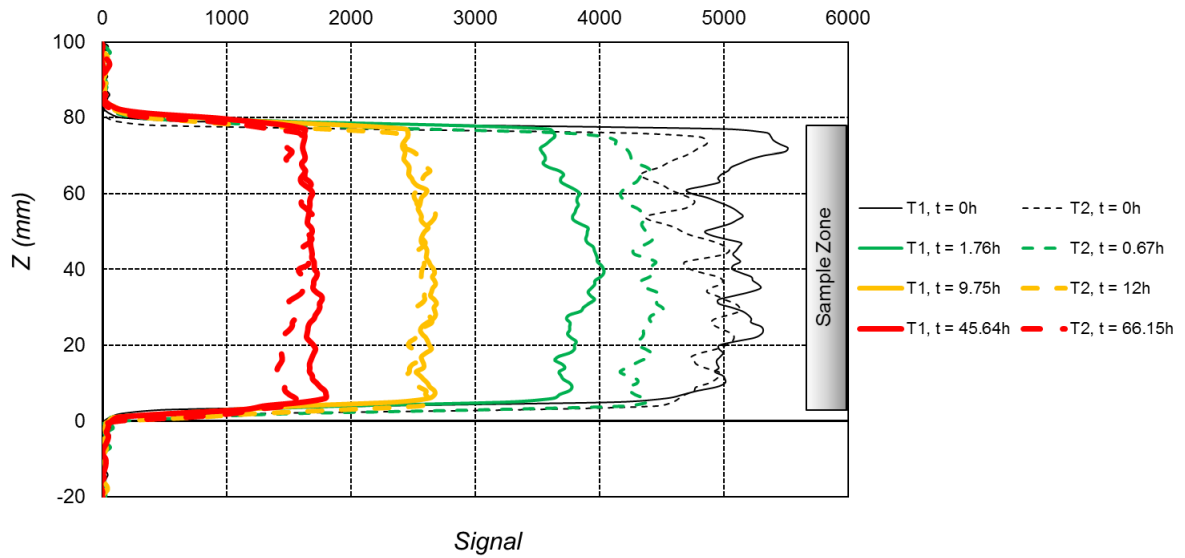


650

651 **Figure 4. (a) FID Intensity evolution of the two tests during GH Formation in gas**
 652 **saturated media; (b) Pore Pressure and (c) Estimated gas hydrate saturation**
 653 **evolution of Test 2.**

654

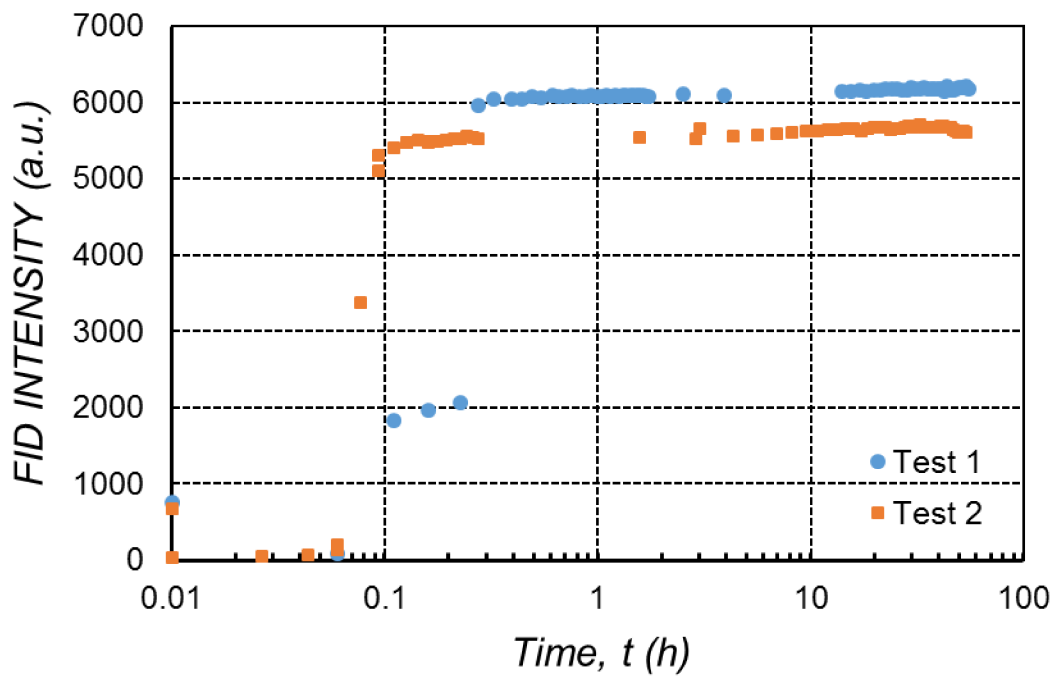
655



656

657 **Figure 5. Signal versus elevation for the two tests during GH formation in gas**
 658 **saturated media**

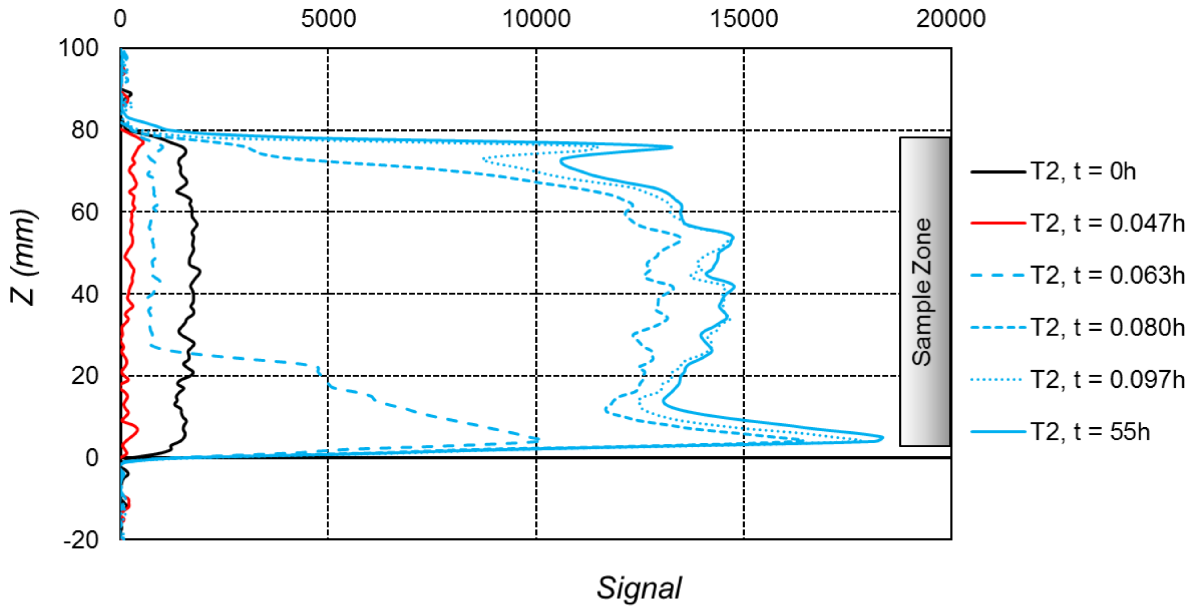
659



660

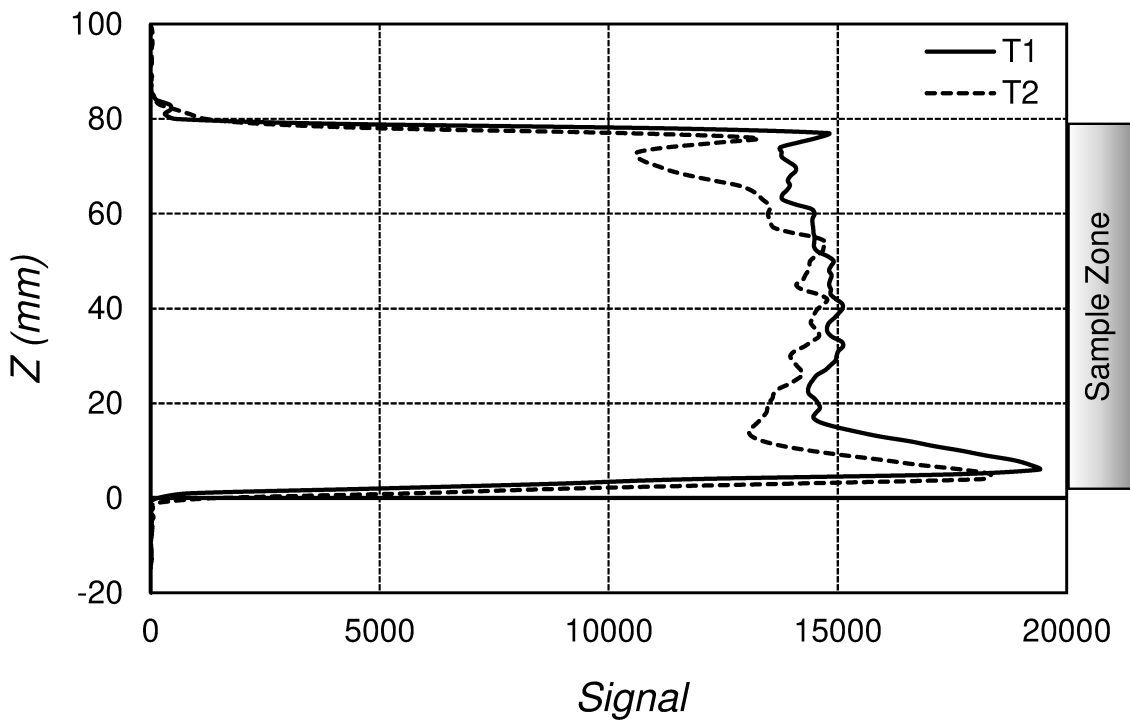
661 **Figure 6. FID Intensity evolution of the two tests during the water saturation**
 662 **process**

663



664
665

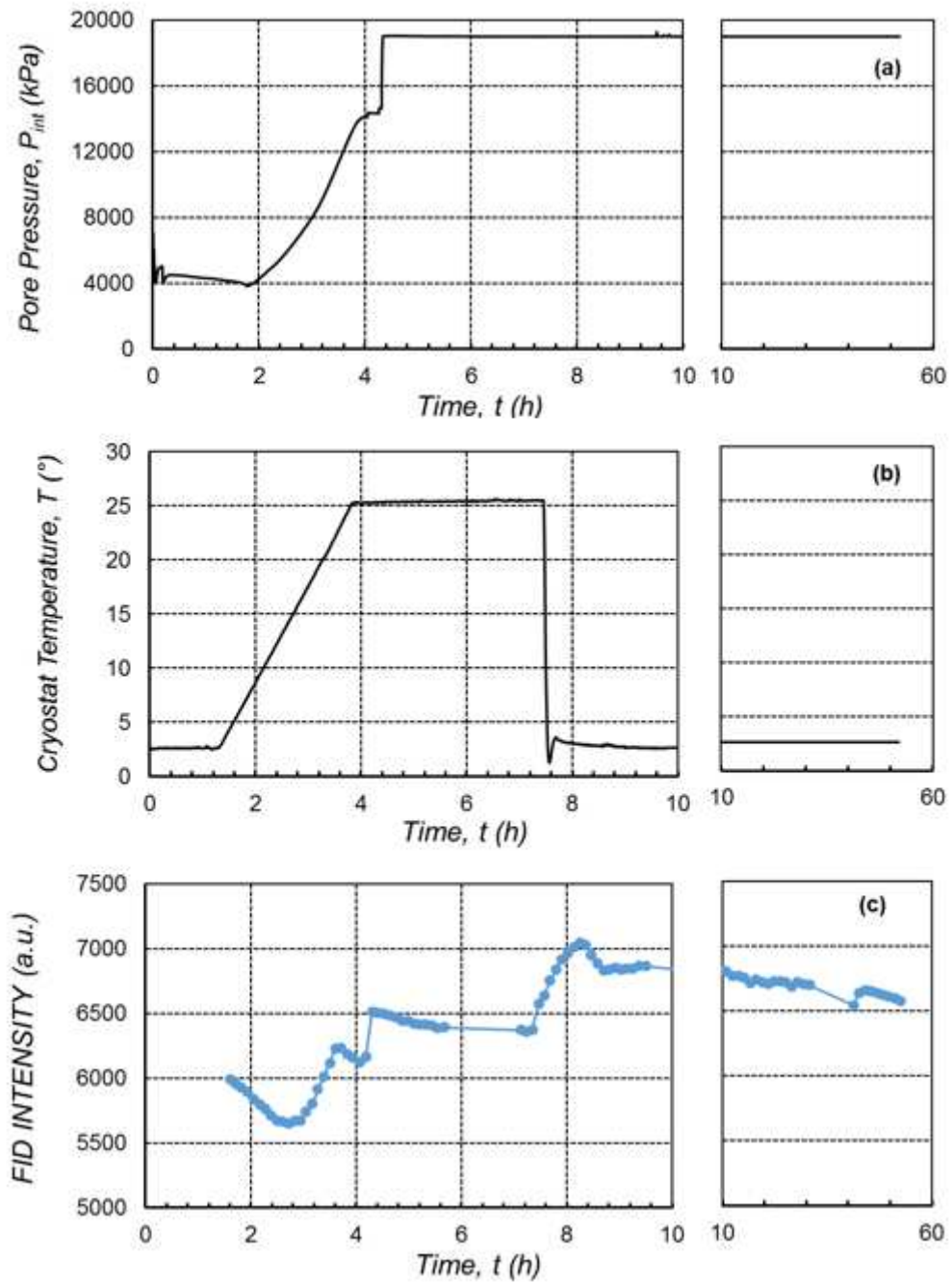
666 **Figure 7. Signal versus elevation for Test 2 during the water saturation process**



667
668
669

Figure 8. Signal versus elevation for the two tests at the end of the water saturation phase

670
671



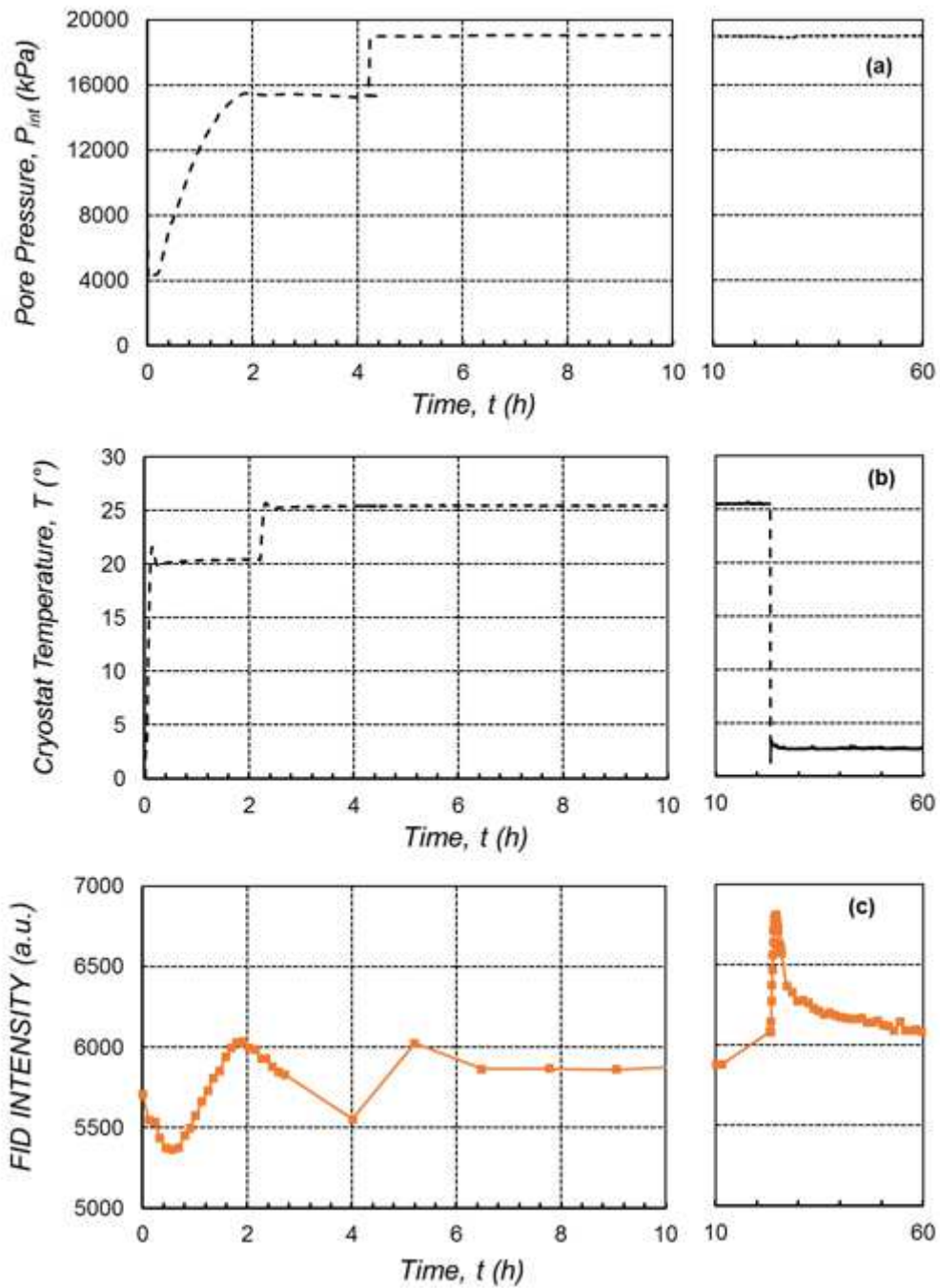
672

673

674

Figure 9. (a) Pressure evolution; (b) –Temperature evolution; (c) FID Intensity evolution during GH dissociation-reformation of Test 1

675



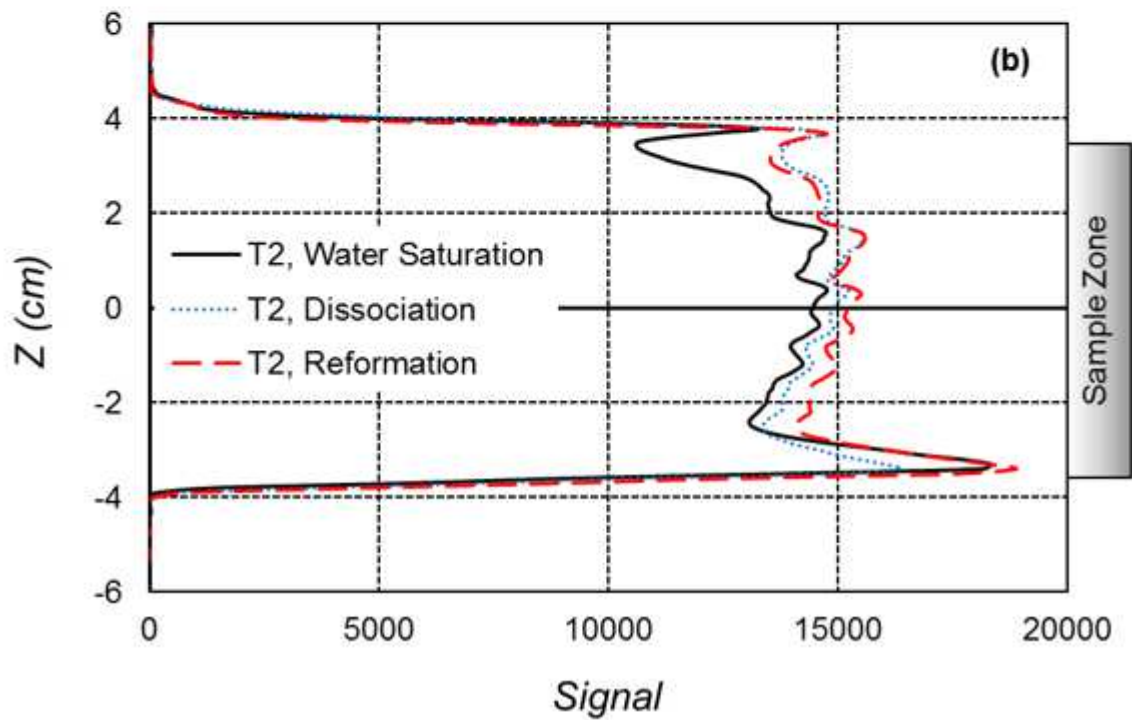
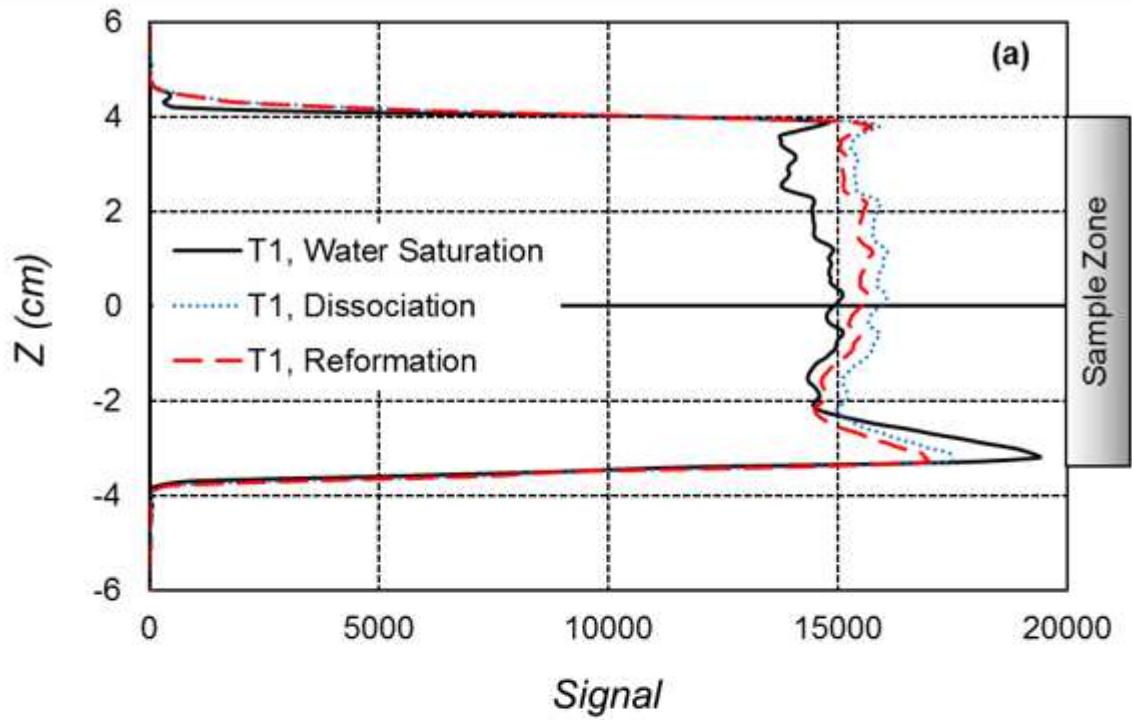
676

677 **Figure 10. (a) Pressure evolution; (b) Temperature evolution; (c) FID Intensity**
 678 **evolution during GH dissociation-reformation of Test 2**

679

680

681



682

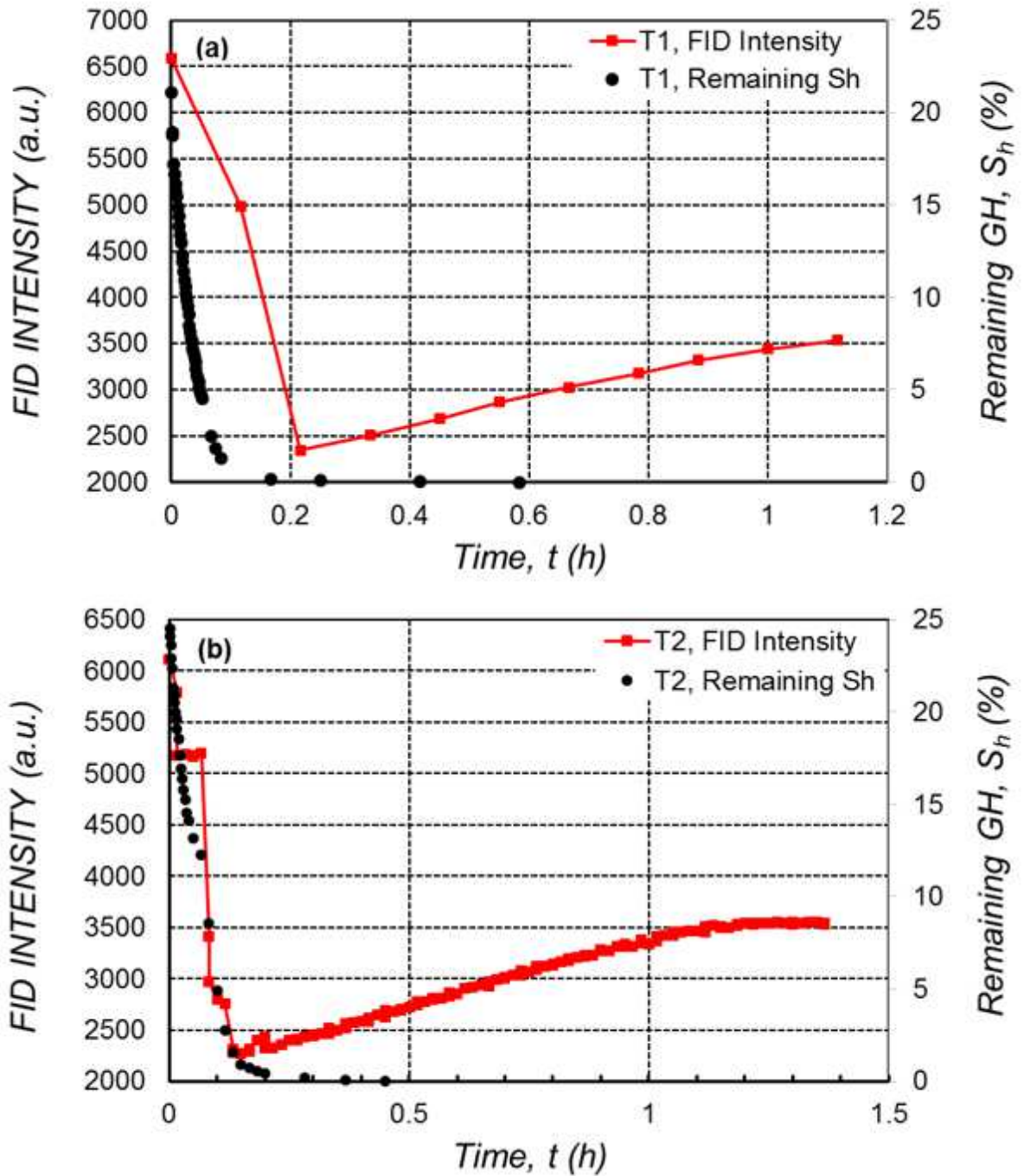
683

684

Figure 11. Signal versus elevation at the end of the water saturation, GH dissociation, and GH reformation phases: (a) Test 1; (b) Test 2.

685

686



687

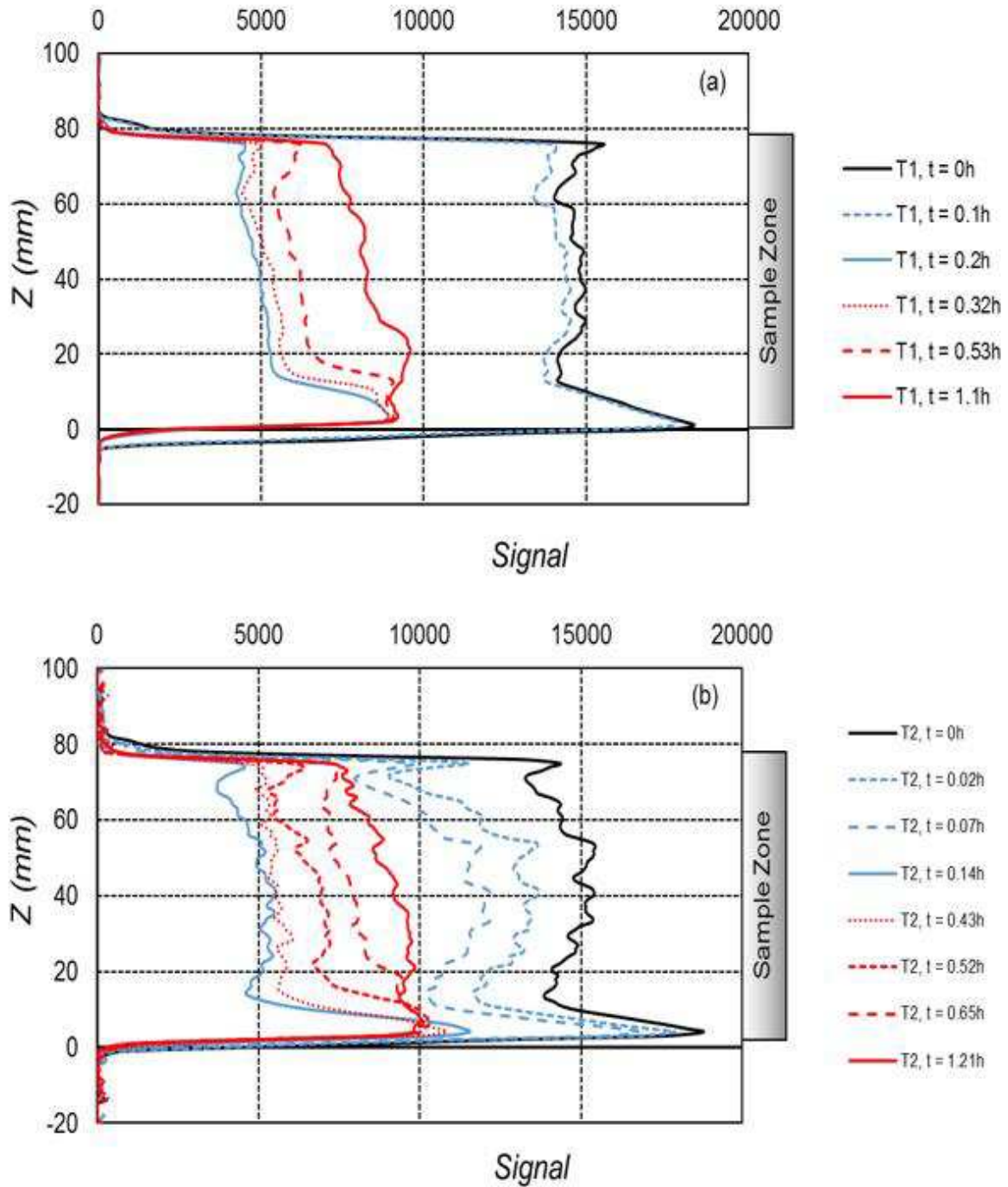
688

689

Figure 12. FID Intensity and Remaining GH evolution during GH dissociation for (a) Test 1 and (b) Test 2.

690

691



692
693

694

Figure 13. Signal versus elevation for the two tests during GH dissociation